Chinese Chemical Letters 34 (2023) 108122

Contents lists available at ScienceDirect

Chinese Chemical Letters

journal homepage: www.elsevier.com/locate/cclet

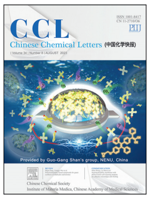

Preparation of novel magnetic noble metals supramolecular composite for the reduction of organic dyes and nitro aromatics

Aadil Nabi Chishti[a], Zhiyuan Ma[a], Junjie Zha[a], Muhammad Ahmad[a,b], Peisen Wang[a], Jagadis Gautam[a], Ming Chen[a], Lubin Ni[a,*], Guowang Diao[a,*]

[a] *School of Chemistry and Chemical Engineering, Yangzhou University, Yangzhou 225002, China*
[b] *College of Environmental Science and Engineering, Yangzhou University, Yangzhou 225002, China*

ARTICLE INFO

Article history:
Received 27 July 2022
Revised 21 December 2022
Accepted 27 December 2022
Available online 28 December 2022

Keywords:
Fe_3O4@SiO_2-Au-Pd@SH-β-*CD* composite
Catalysis
Reduction
Degradation
Synergistic effect

ABSTRACT

By considering the exceptional properties of supramolecular, noble metals (NM) and magnetic nanoparticles (NPs), we successfully synthesized a novel magnetic, metals and supramolecular composite. Briefly, the Fe_3O_4@SiO_2 core-shell spheres were first modified with gold (Au) and palladium (Pd) NPs and then with mono-6-thio-β-cyclodextrin (SH-β-CD). The synthesized Fe_3O_4@SiO_2-Au-Pd@SH-β-CD nanocomposite shows a good magnetic response (42.3 emu/g). The nanocomposite showed good performance for the reductive degradation of rhodamine B (RhB) and 4-nitrophenol (4-NP). The calculated rate constant (k) values for the reduction of 4-NP and RhB were 0.062± 0.02 s^{-1} and 0.027± 0.01 s$^{-1,}$ respectively. The high catalytical performance was supposed to be due to the host-guest interaction of β-CD and also due to the NM synergic effect. The nanocomposite structural and chemical morphology was investigated by various spectroscopic techniques. Furthermore, the catalyst was recycled six times and it maintains morphology, chemical nature, and high magnetic behavior, as demonstrated by FTIR and TEM analysis of the recycled catalyst. These results demonstrate a very efficient, cost-effective, and recyclable catalyst in the field of catalysis technology development.

With the development of industrial technology, the amount of organic pollutants is constantly growing. In particular, water pollution produced by printing and textile factories has seriously affected the environment and caused severe consequences, such as esthetic pollution, toxicity, and perturbation of aquatic life. Rhodamine B (RhB), a positive-charged xanthene dye, is widely used in the textile, paints, paper, plastics, and printing industries [1–4]. It is also exploited as a model dye in many essential biochemical applications due to its well-established chemistry [5,6]. The wide use of RhB for industrial and other purposes results in a large-scale buildup in the environment, particularly in ground and surface water [7]. RhB's unusual chemical structure imparts great chemical and biological stability, making its elimination by natural and chemical degradation extremely challenging. The RhB is a well-known hazardous pollutant linked to carcinogenic and mutagenesis effects in biological systems [8–11]. Excessive RhB aggregation in the water and soil bodies has been shown to impair the photosynthetic cycle in plant metabolism and to produce waterborne diseases such as vomiting, cancer, and bleeding [12]. The toxicity data on RhB that have been published thus far indicate that its large concentrations constitute a significant hazard to human life and as well as to aquatic life. As a result, considerable research efforts have been directed toward developing effective, safe, efficient, cost-efficient, and dependable technologies for the complete removal (reduction) and degradation of RhB from industrial wastes [13–16].

Thus, organic pollutants removal from industrial wastewater is a critical issue, and adequate wastewater treatment should be carried out to reduce the environmental effect. A wide range of wastewater treatment techniques, including chemical and biological approaches such as coagulation/flocculation, electrochemical degradation, photocatalytic degradation, advanced oxidation, and ozonation, have been used. For the treatment of dye-bearing wastewater, membrane filtration and liquid-liquid extraction have been frequently utilized [17–21]. As a result, they are restricted to laboratory applications [22,23]. One of the most promising wastewater treatment techniques for removing colored pollutants is adsorption, which is a valuable approach because of its high removal efficiencies, cheap cost, flexibility in design, ease of operation, and insensitivity to harmful compounds [24]. Adsorption methods have been utilized to remove colors from an aqueous

---

[*] Corresponding authors.
E-mail addresses: lbni@yzu.edu.cn (L. Ni), gwdiao@yzu.edu.cn (G. Diao).

https://doi.org/10.1016/j.cclet.2022.108122

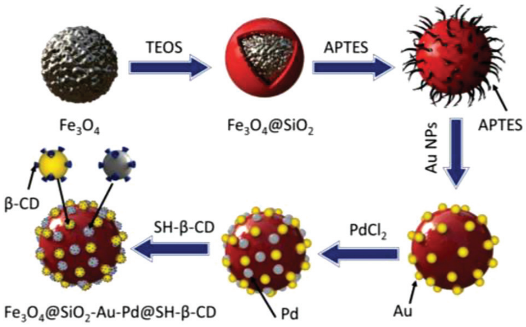

Scheme 1. Schematic synthesis of SH-β-CD modified Fe_3O_4@SiO_2-Au-Pd composite.

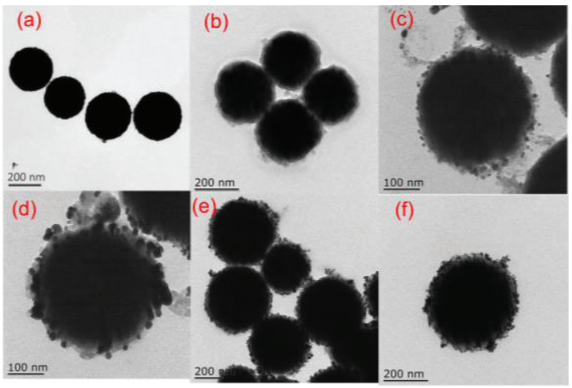

Fig. 1. TEM images of (a) Fe_3O_4, (b) Fe_3O_4@SiO_2, (c) Fe_3O_4@SiO_2-Pd, (d) Fe_3O_4@SiO_2-Au, (e) Fe_3O_4@SiO_2-Au-Pd and (f) Fe_3O_4@SiO_2-Au-Pd@β-CD respectively.

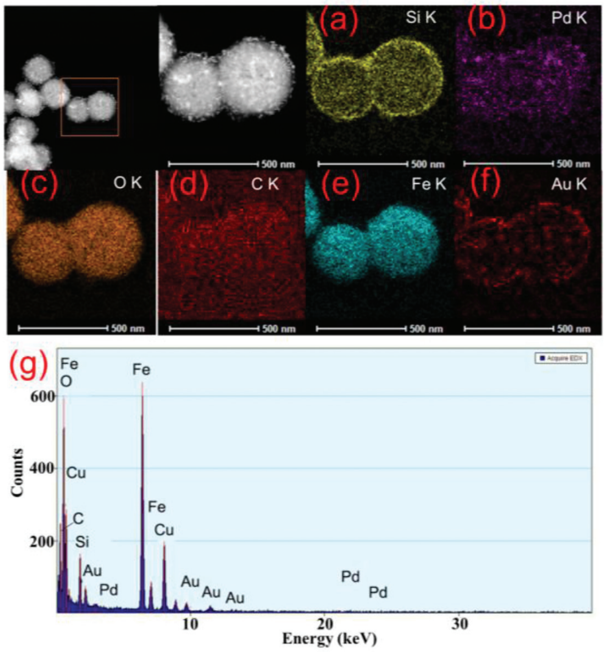

Fig. 2. TEM-EDX analysis. (a-f) Color mapping of different elements and (g) elemental spectrum of different elements in the synthesized nanocomposite.

medium using sorbents derived from organic and inorganic sources with sizes ranging from nano to micro. Several sorbents have been produced to remove dyes, including functionalized membranes, carbon-based materials, nanocomposites, porous polymers, natural clay, fibers and gels [25–27].

The utilization of precious metal nanoparticles has been shown to have good catalytic activity toward the reduction and degradation of RhB and 4-NP [28–31]. Metal nanoparticles' outstanding activity toward RhB reduction and degradation is ascribed to their high surface-to-volume ratio and unique electrical characteristics. Until now, a wide range of heterogeneous catalysts based on metallic nanoparticles (MNPs), bimetallic nanoparticles, and metal oxide nanoparticles (MNOPs) of Ag, Au, Fe, Cu, Ni and Pt have been purposefully designed and extensively tested as catalysts for the $NaBH_4$-induced reductive detoxification of organic pollutants [32–34]. Immobilizing these different MNOPs onto suitable supports is a well-established technique for preventing accumulation and improving catalytic performance, reusability, and stability. Magnetite and its other forms have emerged as impressive nano support for the immobilization of catalytic MNPs, Bi-MNPs, and MNOPs [35–37]. Due to their very high electronic conduction, specific surface area, and inertness in reaction media, among other properties. In our previous work, we synthesized Ag decorated Fe_3O_4@C-TiO_2 nanocomposites which show good catalytic activities. Here in this study, for further enhancing and studying the effect of SH-β-CD along with Au and Pd NPs on the reduction of organic pollutants, cyclodextrins (CDs) are well-known supramolecular hosts, cyclic oligosaccharides with cylindrical cone-shaped cavities. Such a structure has a lipophilic inner surface and a hydrophilic outer surface, allowing a wide variety of organic molecules to be included inside their cavities to create complexation. As inverse phase transfer agents for aqueous biphasic processes, they can transfer hydrophobic molecules from the organic phase to the catalytic species in aqueous environments, resulting in increased solubility of organic material in water [38–40]. We synthesized a novel SH-β-CD modified Fe_3O_4@SiO_2-Au-Pd nanocomposite. The surface of the Fe_3O_4@SiO_2 core-shell structure was first modified with Au and Pd NPs and then with SH-β-CD. The catalytic performance of the synthesized nanocomposite was remarkable for the photodegradation and reduction of both RhB and 4-NP. The obtained results show encouraging catalytic activity, reusability and stability of the synthesized composite.

The synthesis process of Fe_3O_4@SiO_2-Au-Pd@SH-β-CD is shown in Scheme 1 and Scheme S1 (Supporting information). In the first step, Fe_3O_4 NPs were synthesized by the hydrothermal method. In the second step, the surface of Fe_3O_4 was coated with a SiO_2 shell to protect their agglomeration. To increase the capability of Fe_3O_4@SiO_2 towards Au and Pd attachments, the surface of nanoparticles was modified with APTES whose role is a binding bridge between Fe_3O_4@SiO_2 and Au, Pd NPs [42]. The surface of Fe_3O_4@SiO_2 nanospheres was modified with Pd(II) ions and Au, which can be used as a heterogeneous catalyst. Finally, on the surface of Fe_3O_4@SiO_2-Au-Pd microspheres, the mono-6-thio-β-CD (SH-β-CD) was prefabricated *via* Au and Pd-Thiol bond formation, assembling monolayer with chiral surface characteristics [43]. The FTIR analysis was used to prove the successful synthesis of the nanocomposite. Also, the enhanced catalytic activity of β-CD modified magnetic microspheres shows its existence in the composite spheres. The stable structure along with magnetic properties, the synthesized composite guarantees excellent recyclability, stability and catalytic activities.

The morphologies and structures of as-prepared Fe_3O_4, Fe_3O_4@SiO_2, Fe_3O_4@SiO_2-Pd, Fe_3O_4@SiO_2-Au, Fe_3O_4@SiO_2-Au-Pd and Fe_3O_4@SiO_2-Au-Pd@SH-β-CD nanocomposites were investigated by TEM analysis. The TEM images of Fe_3O_4 NPs show its spherical shape with an average size of 325 nm (Fig. 1a). The Fe_3O_4 core is coated with 21 nm shell of SiO_2, which shield the core and Au and Pd NPs attached to its surface (Fig. 2b). The surface of Fe_3O_4@SiO_2 was modified with Pd and Au NPs as shown in Figs. 1c and d, respectively. Fig. 1e shows the TEM image

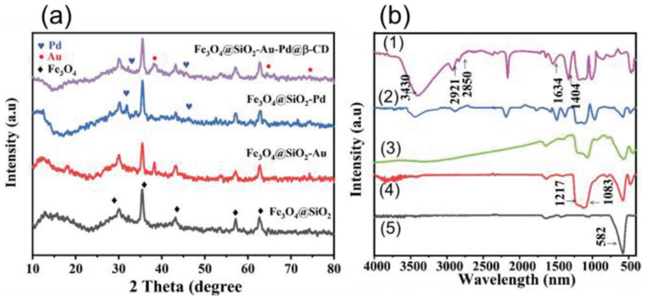

Fig. 3. (a) XRD analysis of $Fe_3O_4@SiO_2$ and $Fe_3O_4@SiO_2$-Au, $Fe_3O_4@SiO_2$-Pd, $Fe_3O_4@SiO_2$-Au-Pd@β-CD respectively. (b) FTIR analysis of (1) Fe_3O_4 (2) $Fe_3O_4@SiO_2$, (3) $Fe_3O_4@SiO_2$-Au-Pd, (4) $Fe_3O_4@SiO_2$-Au-Pd@β-CD and (5) SH-β-CD respectively.

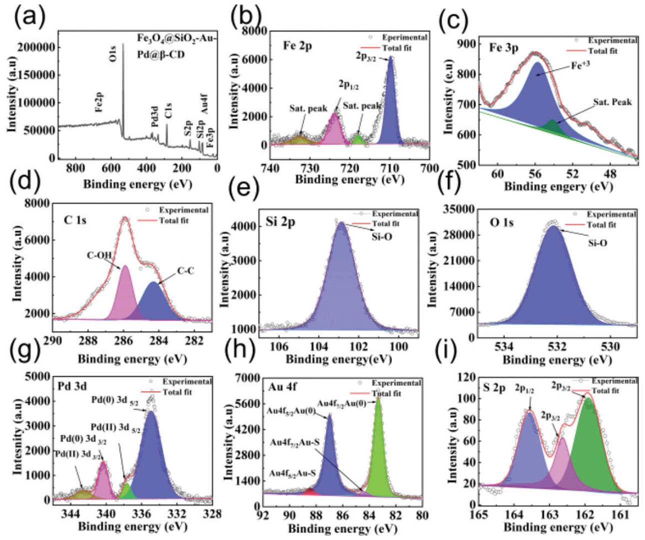

Fig. 4. (a) XPS survey scan of $Fe_3O_4@SiO_2$-Pd-Au@SH-β-CD. (b) High resolution (HR) XPS spectra of Fe 2p. (c) HR XPS spectrum of Fe 3p. (d) C 1s HR XPS spectrum. (e) HR spectrum of Si 2p. (f) HR XPS spectrum of O 1s. (g) HR XPS spectrum of Pd 3d (h) HR spectrum of Au 4f and (i) HR XPS spectrum of S 2p.

of $Fe_3O_4@SiO_2$-Au-Pd nanocomposite. The core-shell structure was successfully modified with Pd and Au NPs as it can be seen from the TEM analysis the number of small NPs on the surface of SiO_2 increased as compared to Figs. 1c and d. TEM analysis of $Fe_3O_4@SiO_2$-Au-Pd-SH-β-CD is shown in Fig. 1f, and there is no such difference between (e) and (f), the dynamic light scattering analysis (DLS) and TEM images at 1 µm magnification are given in Fig. S1 (Supporting information). The synthesized $Fe_3O_4@SiO_2$-Au-Pd-SH-β-CD composite was further investigated by TEM-EDX analysis.

Fig. 2 shows the TEM-EDX analysis of $Fe_3O_4@SiO_2$-Au-Pd@SH-β-CD nanocomposites. The TEM EDX elemental mapping of Fe, O, Si, Pd, Au and C show a spatial distribution of all elements and their position in the synthesized nanocomposite as shown in Figs. 2a-f. Different colors represent different elements of the nanocomposite. The EDX spectrum of $Fe_3O_4@SiO_2$-Au-Pd@SH-β-CD composite is given in Fig. 2g. Significant peaks for iron, oxygen, carbon, silicon, palladium and gold were observed, which suggest the successful synthesis of core-shell $Fe_3O_4@SiO_2$-Au-Pd@SH-β-CD nanocomposite [44].

The XRD patterns of the synthesized nanocomposite are shown in Fig. 3a. The XRD pattern of $Fe_3O_4@SiO_2$-Au-Pd@SH-β-CD was compared with Fe_3O_4, $Fe_3O_4@SiO_2$, $Fe_3O_4@SiO_2$-Au and $Fe_3O_4@SiO_2$-Au-Pd. The XRD pattern of Fe_3O_4 and $Fe_3O_4@SiO_2$ are almost the same and peaks at 2θ of 30.2°, 35.5°, 43.4°, 53.1°, 57.2° and 62.6° which are attributed to (220), (311), (400), (422), (511), (440) and (533) reflections planes respectively (PDF#19–629). $Fe_3O_4@SiO_2$-Au XRD pattern shows peaks $2\theta = 38.1°$, 44.2° and 64.5° which are attributed to (111), (200) and (220) diffraction planes of Au in the cubic phase [44]. Similarly, the XRD pattern of $Fe_3O_4@SiO_2$-Pd shows peaks at 2θ 46.3° and 32.2°, which are related to (200) and (111) reflection planes, respectively [45,46]. The XRD analysis of $Fe_3O_4@SiO_2$-Au-Pd@SH-β-CD composite showed all the peaks associated to Fe_3O_4. Au and Pd with slightly decreased intensities, which suggests the surface of $Fe_3O_4@SiO_2$-Au-Pd was modification with SH-β-CD.

The successful synthesis of $Fe_3O_4@SiO_2$-Au-Pd modified with SH-β-CD was verified by FTIR spectroscopic analysis. Fig. 3b shows the FTIR spectra of Fe_3O_4, $Fe_3O_4@SiO_2$, $Fe_3O_4@SiO_2$-Au-Pd, $Fe_3O_4@SiO_2$-Au-Pd@SH-β-CD and SH-β-CD. The peak at 581 cm^{-1} is assigned to Fe-O-Fe and 1084–1218 cm^{-1} is assigned to the absorption Si-O-Si vibration. The absorption peaks at 3430 and 1634 cm^{-1} are attributed to the O–H stretching vibration of SiO_2, adsorbed water, or β-CD. Peaks at 2921 and 2850 cm^{-1} were assigned for asymmetric and symmetric stretching vibrations of SH-β-CD. By comparing the FTIR spectrum of $Fe_3O_4@SiO_2$-Au-Pd and $Fe_3O_4@SiO_2$-Au-Pd@β-CD, new peaks at 2921 and 1404 cm^{-1} were observed. The appearance of the new peaks was correlated to the SH-β-CD mole fraction in the self-assembled monolayer and hence, the observed changes indicate the successful modification of $Fe_3O_4@SiO_2$-Au-Pd surface with β-CD as it shows a similar FTIR pattern as SH-β-CD (Fig. 3b, curve 5).

The XPS analysis was carried out for the synthesized $Fe_3O_4@SiO_2$-Au-Pd@β-CD nanocomposite, as shown in Fig. 4. The survey spectra for the synthesized composite are illustrated in Fig. 4a. The surface elemental concentration for O 1s, C 1s, Si 2p, Pd 3d, Au 4f and S 2p were 44.37%, 33.55%, 14.74%, 0.76%,1.1% and 2.3% respectively. The high resolution XPS spectrum for Fe 2p is shown in Fig. 4b, which shows two high intensity peaks with binding energies at 709.8 eV and 723.8 eV attributed to $2p_{3/2}$ and $2p_{1/2}$, respectively. The satellite peaks were observed at binding energy 717.8 eV and 732.6 eV. The Fe 3p high resolution spectrum is given in Fig. 4c, which shows two peaks at binding energy 55.73 and 53.9, attributed to Fe(III) and satellite peak, respectively [47–49]. The C 1s spectrum is shown in Fig. 4d. The high intensity peak at binding energy 285.9 eV is assigned to C–O bond and other C=C bonds, while the peak at binding energy 284.3 eV is attributed to C=C bond [47]. High resolution XPS spectrum for Si 2p is shown in Fig. 4e, which shows a high intensity peak at binding energy 102.9 eV attributed to Si-O bond [50]. The O 1s spectrum shows peak at binding energy 532.12 eV which is attributed to Si-O and Fe-O bond (Fig. 4f) [51]. The chemical and electronic structure of thiol-functionalized palladium and gold nanoparticles were also analyzed. As shown in Fig. 4g, the Pd 3d spectrum shows two types of valence state Pd, strong peaks at 334.9 eV and 340.32 eV could be assigned to Pd(0) and the two other peaks which are comparatively weak, allocated at 337.7 eV and 342.6 are attributed to Pd(II) [52,53]. The Au 4f shows two types of peaks (Fig. 4h). The Au $4f_{7/2}$ and Au $4f_{5/2}$ at binding energy values of 83.3 eV and 87.02 eV are assigned to metallic Au respectively. The Au $4f_{7/2}$ and Au $4f_{5/2}$ components at binding energy 84.4 eV and 88.5 eV can be attributed to the Au atoms that are covalently bonded to sulfur terminal groups SH-β-CD [54]. The spectra of Pd 3d and Au 4f region were also compared with the nanocomposite before modification of SH-β-CD and the peak for Pd(II) and Au(II) at 342.6 eV and 84.4 were not observed. In the S 2p spectrum (Fig. 4i), the peaks at 163.56 eV and 162.63 eV can be assigned to S(0), which shows Pd-S and Au-S bond formation, and another peak located at 161.9 eV could be attributed to S^{2-} [53]. For the comparison, the XPS analysis of $Fe_3O_4@SiO_2$-Au-Pd was also carried out and shown in Fig.

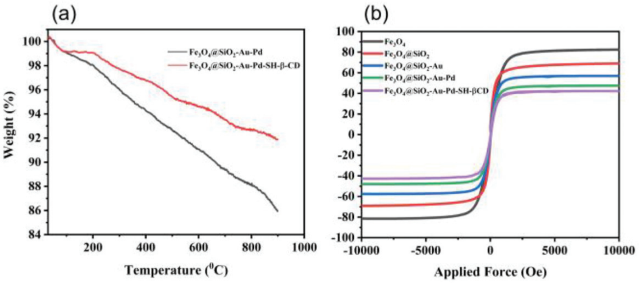

Fig. 5. (a) TGA analysis of Fe_3O_4@SiO_2-Au-Pd and Fe_3O_4@SiO_2-Au-Pd@β-CD. (b) VSM analysis of Fe_3O_4, Fe_3O_4@SiO_2, Fe_3O_4@SiO_2-Au, Fe_3O_4@SiO_2-Au-Pd and Fe_3O_4@SiO_2-Au-Pd@β-CD nanocomposite respectively.

S2 (Supporting information), which shows no sulfur peaks and different oxidation states for Pd and Au NPs. All these results indicate the successful synthesis of the SH-β-CD modified composite.

For the photocatalytic reaction, the light absorption by the material plays a key role along with light-induced electrons and these properties depend on the electronic structure of the materials. The UV–vis spectrum of powder Fe_3O_4@SiO_2-Pd, Fe_3O_4@SiO_2-Pd-Au, and Fe_3O_4@SiO_2-Pd-Au@SH-β-CD was carried measured. The reflectance spectrum and Kubelka Munk *vs.* energy of light plots are given in Fig. S3 (Supporting information). The band gap energy was calculated from Tauc's plot. The formula is based on the energy of the photon, band gap energy and absorption coefficient. The calculated band gap energy for Fe_3O_4@SiO_2-Pd, Fe_3O_4@SiO_2-Pd-Au, and Fe_3O_4@SiO_2-Pd-Au@SH-β-CD were 2.32 eV, 2.09 eV, and 1.99 eV respectively. All the nanomaterials have photo-responsive properties as shown in Figs. S3a, c and e in the visible region. The Touc's plots are given in Figs. S3b, d and g.

The differences in the surface components and stability of the nanomaterials were emphasized further by different weight loss characteristics measurements by TG Analysis. As shown in Fig. 5a, the weight loss in the case of Fe_3O_4@SiO_2-Au-Pd was about 15%, while in the case of Fe_3O_4@SiO_2-Au-Pd-SH-β-CD, the weight loss reduces to approximately 9%. The weight loss in the former NPs is related to some water molecules, residual ethanol, APTES on the surface and might be due to metallic NPs. After modifying the Fe_3O_4@SiO_2-Au-Pd with SH-β-CD, the stability of the synthesized nanocomposites increased and the weight loss decreased, which also showed the successful surface modification of Fe_3O_4@SiO_2-Au-Pd by SH-β-CD [55–57]. The TG analysis of SH-β-CD was also carried out, which reveals the same pattern during weight loss as Fe_3O_4@SiO_2-Au-Pd-SH-β-CD composite Fig. S4 (Supporting information), which also suggests composite surface modification.

The magnetic properties of the synthesized nanocomposites were analyzed by the vibrating sample magnetometer (VSM) technique. The magnetization saturation (MS) values were calculated for all the NPs step by step. The MS values for Fe_3O_4, Fe_3O_4@SiO_2, Fe_3O_4@SiO_2-Pd, Fe_3O_4@SiO_2-Pd-Au, and Fe_3O_4@SiO_2-Pd-Au@SH-β-CD were 80.1, 68.1, 57.2, 47.4 and 42.3 emu/g, respectively (Fig. 5b). This decrease in the MS values also shows the successful surface modification of the synthesized nanocomposites. Although the MS values decreased for Fe_3O_4@SiO_2-Pd-Au@SH-β-CD nanocomposites, it still can be recycled through an external magnetization field.

Before the detailed catalytic studies, we synthesized different catalysts on the basis of $PdCl_2$, $HAuCl_4$ and SH-β-CD concentration. First, the catalytic activities were investigated and the ones with the best result were chosen for all the experiments and characterizations. The details about the concentration and catalytic activities results are shown in Table S1 (Supporting information). For the optimized preparation of SH-β-CD modified Fe_3O_4@SiO_2-Au-Pd nano spheres, various concentrations of SH-β-CD, from 2 mmol/L to 10 mmol/L were used and the amount of Fe_3O_4@SiO_2-Au-Pd was kept constant. The synthesized nanocomposites were named according to the concentration of SH-β-CD. Based on catalytic activities, the one with good performance was used for further analysis and characterization. The catalytic activities result is shown in Fig. 8a.

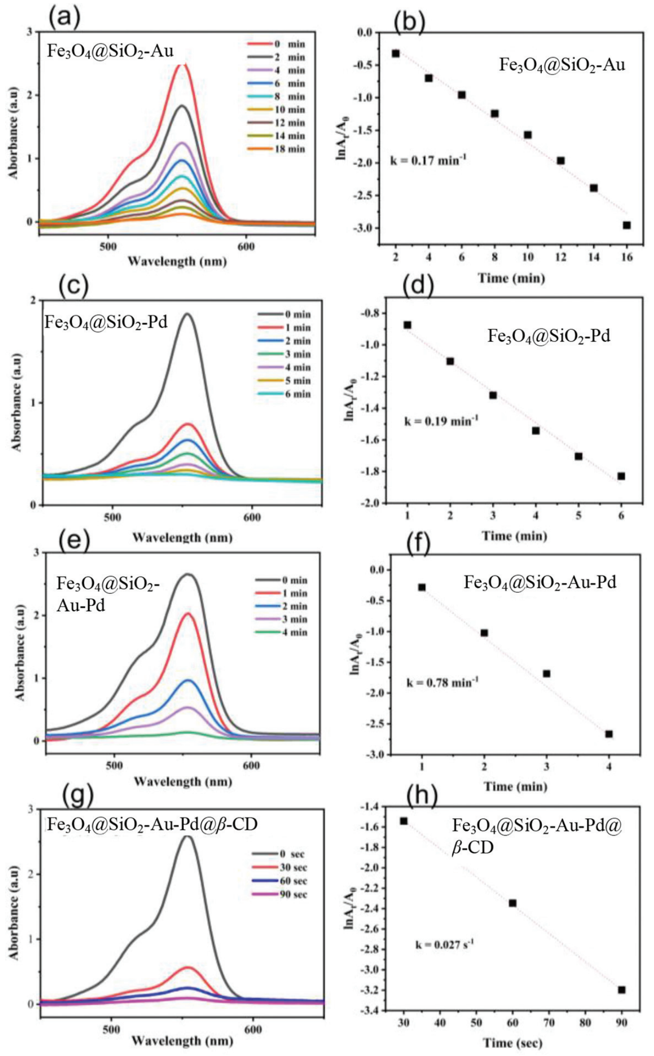

Fig. 6. Time dependent UV–vis absorption spectrum and rate constant for the reduction of RhB in the presence of $NaBH_4$ and (a, b) Fe_3O_4@SiO_2-Au, (c, d) Fe_3O_4@SiO_2-Pd, (e, f) Fe_3O_4@SiO_2-Au-Pd and (g, h) Fe_3O_4@SiO_2-Au-Pd@β-CD nanocomposite respectively. The concentration of RhB and $NaBH_4$ were kept constant. All the experiments were carried out at room temperature.

Recently the reduction of organic molecules in the presence of $NaBH_4$ is an effective and environment-friendly technique. To investigate the synthesised catalyst's activity, the reduction of 4-NP and RhB in the presence of $NaBH_4$ was chosen as a model reaction. The reduction peaks were monitored by UV–vis spectrophotometer at 400 nm and 554 nm for 4-NP and RhB, respectively. The results show that the time required for the reduction of 4-NP and RhB is different for different catalysts at room temperature. In the reduction reaction, the color disappeared and the solutions turned colorless. The peaks at 400 nm and 554 nm decrease with time, as shown in Figs. 6 and 7. The reduction was also carried out only in the presence of $NaBH_4$ and even after a long time, no such changes were observed, which shows that the reduction cannot proceed without the proper catalyst. Many groups have reported

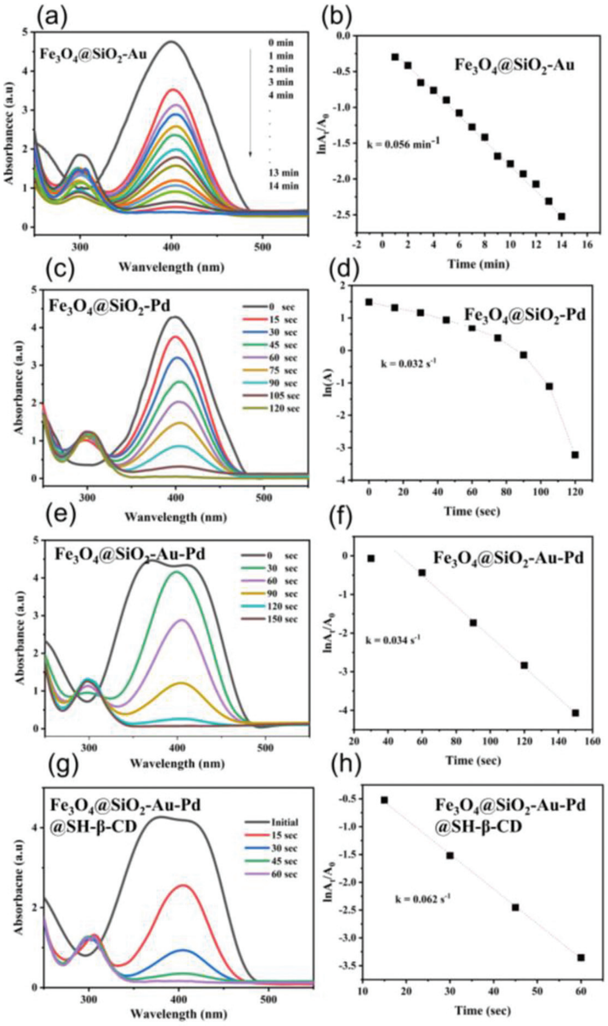

Fig. 7. Time dependent UV–vis absorption spectrum and rate constant for the reduction of 4-NP in the presence of $NaBH_4$ and (a, b) Fe_3O_4@SiO_2-Au, (c, d) Fe_3O_4@SiO_2-Pd, (e, f) Fe_3O_4@SiO_2-Au-Pd and (g, h) Fe_3O_4@SiO_2-Au-Pd@β-CD nanocomposite respectively. The concentrations of RhB and $NaBH_4$ were kept constant. All the experiments were carried out at room temperature.

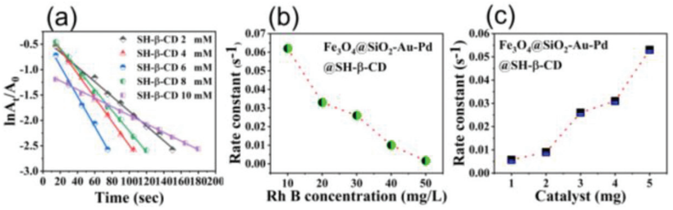

Fig. 8. (a) $\ln A_t/\ln A_0$ values for the reduction of RhB using Fe_3O_4@SiO_2-Au-Pd@β-CD catalysts synthesized based on various SH-β-CD concentrations. (b) Rate constants value for RhB reduction at constant catalyst concentration (2 mg) and different RhB concentration (c) at constant RhB concentration (30 mg/L) and different catalyst mass respectively.

similar observations about the reduction of RhB and 4-NP in the past [15,58,59]. Similarly, Fe_3O_4 and Fe_3O_4@SiO_2 were also used for the reduction of RhB and 4-NP but a very small change in the reduction spectra was observed, these results suggest a suitable catalyst for the reduction of RhB and 4-NP. The spectra were recorded for the reduction of RhB under different synthesized catalysts and $NaBH_4$ (Figs. 6a, c and e). The reduction of RhB was completed in 18, 6 and 4 min when 1 mg of Fe_3O_4@SiO_2-Au, Fe_3O_4@SiO_2-Pd and Fe_3O_4@SiO_2-Au-Pd were added, respectively, which indicates that the Fe_3O_4@SiO_2-Au-Pd composite has high catalytic performance due to the presence of Au and Pd nanoparticles. After the surface modification of Fe_3O_4@SiO_2-Au-Pd with SH-β-CD, the catalytic activity enhanced (Fig. 6g), and the reduction process was completed in 90s, which also proves the successful loading of SH-β-CD molecule on the composite surface. The synthesized composite was also used as a photocatalyst for the degradation of RhB, under the irradiation of visible light and it shows good activity. The degradation reaction was completed in 35 min with a rate constant value of 0.046 ± 0.007 min^{-1} (Fig. S5 in Supporting information).

It was observed that the pink color of RhB solution changed to a colorless solution. The $NaBH_4$ was used in excess as it has no such effect on the reduction of RhB. The rate constants were calculated from the absorption peak and time interval. The first order kinetics equation can be written as:

$$\ln(A_t/A_0) = -kt \tag{1}$$

where A_0 is initial absorbance, A_t is absorbance after time t, and k is rate constant for the first order reaction. The kinetics plots for different catalysts are presented in Figs. 6b, d, f and h. The given data fit well to first-order law and the value of R^2 is almost 0.99 for all. The presented assumption was proven correct that RhB reduction follows first-order kinetics rate law. The calculated rate constants in the presence of Fe_3O_4@SiO_2-Au, Fe_3O_4@SiO_2-Pd, Fe_3O_4@SiO_2-Au-Pd and Fe_3O_4@SiO_2-Au-Pd@SH-β-CD were 0.017 ± 0.005 min^{-1}, 0.19 ± 0.0002 min^{-1}, 0.78 ± 0.001 min^{-1} and 0.027 ± 0.01 s^{-1} respectively.

A similar study was carried out for the reduction of 4-NP in the presence of different synthesized catalysts and $NaBH_4$. The UV–vis absorption spectra and rate constant patterns under different synthesized catalysts are shown in Figs. 7a-h. The rate constants values for the reduction of 4-NP to 4-AP are 0.056 ± 0.0032 min^{-1}, 0.036 ± 0.0043 s^{-1}, 0.034 ± 0.001 s^{-1} and 0.062 ± 0.003 s^{-1} in the presence of Fe_3O_4@SiO_2-Au, Fe_3O_4@SiO_2-Pd, Fe_3O_4@SiO_2-Au-Pd and Fe_3O_4@SiO_2-Au-Pd@SH-β-CD nanocomposites respectively, which indicates that SH-β-CD modified Fe_3O_4@SiO_2-Au-Pd shows better performance like it shows in case of RhB reduction.

Catalyst dosage at constant RhB (30 mg/L) concentration was also investigated. Increasing the amount of catalyst increases the reduction of RhB and the rate constant values also increase as shown in Fig. 8c. The rate constant value was observed to decrease when the concentration of the catalyst was held constant while the concentration of RhB was changed, as illustrated in Fig. 8b. This tendency in the change of k with increasing RhB concentration can be explained by catalyst surface saturation at greater concentrations of the RhB.

The reduction of RhB by $NaBH_4$ is well acknowledged, as the electrons transfer involves between RhB and $NaBH_4$, however, the considerable variation in their reduction potential considerably impedes the electrons transfer and the kinetics of the solution. Metal catalysts have been shown to operate as an intermediary between the high redox potentials of RhB and $NaBH_4$ by propagating electrons between BH_4^- and RhB [60,61]. Generally, metal nano particles possess a negative charge while RhB is positively charged, as a result, RhB is absorbed on the metal surface, at neutral pH. In general, the surface catalyzed reduction of big molecules such as dyes is mostly related to their adsorption and desorption on the catalyst surface. Metal nanoparticles serve as electron bridges between BH_4^- and RhB, with BH_4^- providing electrons to metal nanoparticles, which transfer the electrons to RhB and reduction takes place [12,62]. The catalytic activity of Fe_3O_4@SiO_2-Au-Pd@SH-β-CD is much higher than that of Fe_3O_4@SiO_2-Au-Pd which is due to the participation of β-CD cavities and the binding sites uptakes RhB molecules through host-guest interaction.

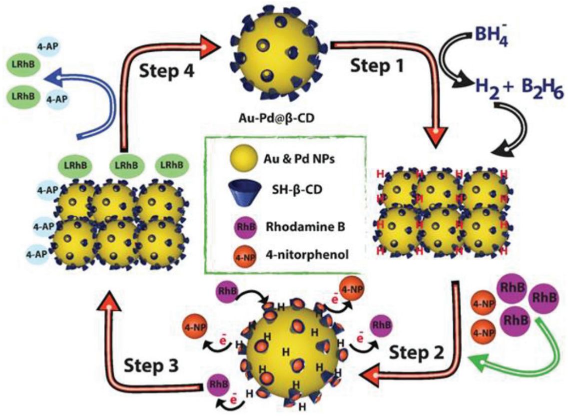

Scheme 2. The schematic diagram and pathway for the reduction mechanism of RhB and 4-NP in the presence of Fe_3O_4@SiO_2-Au-Pd@SH-β-CD composite.

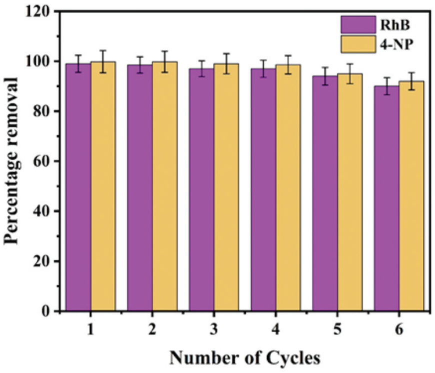

Fig. 9. The number of cycles for RhB and 4-NP reduction using synthesized composite at room temperature.

The mechanism of RhB catalytic reduction in the presence of $NaBH_4$ and catalyst can be explained in the following steps: the $NaBH_4$ (reducing agent) transfers BH_4^- to the catalyst surface, which makes a covalent linkage between catalyst and hydrogen. The second step is the rate-determining step in which the RhB is adsorbed on the catalyst surface. In the third step, the reduction of RhB molecules takes place by seizing electrons from the catalyst active sites and adsorbed hydrogen and also some of the molecules are adsorbed directly to the cavity of SH-β-CD by host-guest interaction. To understand the role and effect of SH-β-CD on the reduction or adsorption of RhB, the reduction experiment was carried out using SH-β-CD solution only. The result shows that in the presence of $NaBH_4$ and SH-β-CD the reduction reaction took place (Fig. S6 in Supporting information), from which we can suppose that some of the RhB molecules make complexes with SH-β-CD [63] or maybe absorbed directly in the cavity of SH-β-CD molecule by the host-guest interaction. In the next step, the desorption of the reduced RhB from the catalyst surface makes the catalyst surface and active sites free for more catalytic activity. The second step in which the adsorption of RhB molecules and 4-NP on the surface of the catalyst is the slow step and rate determined step in the reduction of RhB and 4-NP in the previous studies, in this study the adsorption step is likely faster due to the interaction of RhB and 4-NP with the hydrogen bound on the surface of the catalyst and also due to SH-β-CD presence. On the other hand, the activity of Fe_3O_4@SiO_2-Au is less than that of Fe_3O_4@SiO_2-Au-Pd because of the low affinity of Au alone but after being decorated along with Pd its affinity towards hydrogen further increased. The mechanism of the reduction process is illustrated in Scheme 2.

The chemical oxygen demand (COD) was widely used to measure the organic strength of wastewater. The COD of the RhB solution was measured at different time intervals. The decreased COD values of the treated dye solution indicate the mineralization of the dye molecules. The obtained COD result of RhB is presented in Fig. S7 (Supporting information), which shows the degradation of the dye taking place. In the present work maximum 89% degradation efficiency was obtained.

The stabilization and recyclability of heterogeneous catalysts, particularly those based on nanocomposite materials, are crucial to their practical performance, efficiency, and usefulness. The catalytic performance of Fe_3O_4@SiO_2-Au-Pd@SH-β-CD nanocomposites in multiple catalytic cycles was evaluated to determine their stabilization and recyclability in the $NaBH_4$ induced reduction of RhB and 4-NP. The experiment was carried out by reusing the catalyst for multiple catalytic cycles in a row. Following each catalytic cycle, the composite was separated by an external magnet and repeatedly washed with 0.05 mol/L HCl and water to remove unreacted reactants from its surface. A representative set of observations regarding the usage of Fe_3O_4@SiO_2-Au-Pd@SH-β-CD nanocomposite in several RhB and 4-NP reduction reaction combinations is shown in Fig. 9.

The efficiency for RhB and 4-NP reduction decreased after six cycles from 99% to 90% and 99.6% to 92%, respectively. This clearly shows that the Fe_3O_4@SiO_2-Au-Pd@SH-β-CD nanocomposite catalyst retains significant catalytic activity after numerous cycles.

The RhB and 4-NP catalytic reduction by metal nanoparticles (MNPs) and supported MNP composites have received considerable

Table 1
Comparison of some already reported catalysts with the synthesized catalyst in this study.

Compound	Catalysts	Rate constant	Order of reaction	Ref.
RhB	Gg-cl-P(AA-*co*-AAm)/Fe_3O_4	0.067 min^{-1}	2nd	[64]
	Fe_3Pt-120 mL Ag	0.21 min^{-1}	1st	[65]
	Cu/Fe_3O_4@C	0.96 min^{-1}	1st	[66]
	Fe_3O_4–poly(4-MS-DVB-GMA)–PAMAM-G(2)-AuNPs	0.035 min^{-1}	1st	[67]
	Fe_3O_4@TA/Ag	0.0516 s^{-1}	1st	[68]
	Pd/Fe_3O_4@γ-AlOOH-YSMs	0.018 s^{-1}	1st	[69]
	Fe_3O_4@SiO_2-Au-Pd@SH-β-CD	0.027 ± 0.02 s^{-1}	1st	This work
4-NP	Pd/Fe_3O_4@γ-AlOOH-YSMs	0.037 s^{-1}	1st	[69]
	Cu/Fe_3O_4/eggshell	0.72 min^{-1}	1st	[70]
	Fe_3O_4@TA/Ag	0.0436 s^{-1}	1st	[68]
	Fe_3O_4@C/Ag	0.044 min^{-1}	1st	[41]
	TiO_2@C–Ni	0.60 min^{-1}	1st	[71]
	Fe_3O_4@C-TiO_2-Ag	0.063 s^{-1}	1st	[72]
	Fe_3O_4@SiO_2-Au-Pd@SH-β-CD	0.062 ± 0.01 s^{-1}	1st	This work

attention. Table 1 compares the catalytic efficiency of numerous catalysts reported in the literature previously based on rate constant values [41,64–72]. The table shows that the values of the rate constant of Fe_3O_4@SiO_2-Au-Pd@SH-β-CD catalyst is higher than already reported catalysts. The stability, reusability and catalytic performance of the synthesized nanocomposite are very high as shown by the FTIR and TEM of the recycles catalyst Fig. S8 (Supporting information), which suggests that Fe_3O_4@SiO_2-Au-Pd@SH-β-CD nanocomposite can find encouraging applications in heterogeneous catalysis fields like wastewater treatment and other issues related to the environment.

In the present work, an efficient approach was carried out for the preparation of Fe_3O_4@SiO_2-Au-Pd@SH-β-CD composite by immobilizing $HAuCl_4$, $PdCl_2$ and SH-β-CD over magnetic Fe_3O_4@SiO_2 core-shell structure, and its catalytic performance for the reduction of 4-NP and RhB were examined. SH-β-CD modified Fe_3O_4@SiO_2-Au-Pd nanocomposite showed increased stability and activities as compared to Fe_3O_4@SiO_2-Au-Pd due to the host-guest interaction between RhB and 4-NP molecule and cyclodextrin cavity. Most of the characteristics of SH-β-CD modified Fe_3O_4@SiO_2-Au-Pd nanocomposite remain the same after multiple catalytic performances and no change in the structure of the catalyst was observed. The catalyst can show a vital role in the field of catalysis in the future.

Declaration of competing interest

The authors declare that they have no known competing financial interests or personal relationships that could have appeared to influence the work reported in this paper.

Acknowledgments

This work was supported by the National Natural Science Foundation of China (Nos. 21971221, 21401162, 21773203), the Yangzhou University Interdisciplinary Research Foundation for Chemistry Discipline of Targeted Support (No. yzuxk202010), ‘Qing Lan Project’ in Colleges and Universities of Jiangsu Province, High-Level Entrepreneurial and Innovative Talents Program of Yangzhou University, and the Lvyangjinfeng Talent Program of Yangzhou.

References

[1] K. Yu, S. Yang, C. Liu, et al., Environ. Sci. Technol. 46 (2012) 7318–7326.
[2] S. Han, Y. Cheng, S. Liu, et al., Angew. Chem. Int. Ed. 133 (2021) 6452–6455.
[3] Y. Zhou, Z. Liu, G. Qiao, B. Tang, P. Li, Chin. Chem. Lett. 32 (2021) 3641–3645.
[4] X. Zhang, T. Ren, F. Yang, L. Yuan, Chin. Chem. Lett. 32 (2021) 3890–3894.
[5] Z. Xia, L. Wang, Q. Zhang, F. Li, L. Xu, Polyoxometalates 1 (2022) 9140001.
[6] X. Yang, H. Zhong, Y. Zhu, et al., J. Mater. Chem. 2 (2014) 9040–9047.
[7] U. Rajaji, M. Govindasamy, S.M. Chen, et al., Compos. B: Eng. 152 (2018) 220–230.
[8] B. Sriram, M. Govindasamy, S.F. Wang, et al., Ultrason. Sonochem. 58 (2019) 104618.
[9] J.N. Tiwari, K. Mahesh, N.H. Le, et al., Carbon 56 (2013) 173–182.
[10] X. Zhang, L. Wang, N. Li, Y. Xiao, Chin. Chem. Lett. 32 (2021) 2395–2399.
[11] X. Li, H. Wang, Y. Zhang, Q. Cao, Y. Chen, Chin. Chem. Lett. 32 (2021) 1541–1544.
[12] Y. Zhang, P. Zhu, L. Chen, et al., J. Mater. Chem. 2 (2014) 11966–11973.
[13] Y. Gu, Q. Li, D. Zang, et al., Angew. Chem. Int. Ed. 60 (2021) 13310–13316.
[14] A.K. Abay, X. Chen, D.H. Kuo, New J. Chem. 41 (2017) 5628–5638.
[15] T. Jeyapragasam, R.S. Kannan, Russ. J. Phys. Chem. A 90 (2016) 1334–1337.
[16] O.A. Zelekew, D.H. Kuo, Phys. Chem. Chem. Phys. 18 (2016) 4405–4414.
[17] M. Sulyman, J. Namiesnik, A. Gierak, Pol. J. Environ. Stud. 26 (2017) 479–510.
[18] J. Lu, K. Xu, J. Yang, Y. Hao, F. Cheng, Carbohydr. Polym. 173 (2017) 28–36.
[19] T. Wen, J. Wang, S. Yu, et al., ACS Sustain. Chem. Eng. 5 (2017) 4371–4380.
[20] V. Nayak, M. Jyothi, R.G. Balakrishna, M. Padaki, S. Deon, J. Hazard. Mater. 331 (2017) 289–299.
[21] A.H. Jawad, K. Ismail, M.A.M. Ishak, L.D. Wilson, Chin. J. Chem. Eng. 27 (2019) 1716–1727.
[22] A.H. Jawad, R. Razuan, J.N. Appaturi, L.D. Wilson, Surf. Interfaces 16 (2019) 76–84.
[23] F. Ren, Z. Li, W. Z, et al., J. Colloid Interface Sci. 532 (2018) 58–67.
[24] X.S. Hu, R. Liang, G. Sun, J. Mater. Chem. 6 (2018) 17612–17624.
[25] Z. Wei, Z. Wu, S. Ru, L. Ni, Y. Wei, Chem. J. Chin. Univ. 43 (2022) 20210665.
[26] K. Qin, D. Zang, Y. Wei, Chin. Chem. Lett. 34 (2022) 107999.
[27] Y. Chen, Y. Long, Q. Li, X. Chen, X. Xu, Int. J. Biol. Macromol. 126 (2019) 107–117.
[28] G. Sharma, P. Jeevanandam, Eur. J. Inorg. Chem. 2013 (2013) 6126–6136.
[29] J. Han, P. Fang, W. Jiang, L. Li, R. Guo, Langmuir 28 (2012) 4768–4775.
[30] X. Zhang, M. Lin, X. Lin, et al., ACS Appl. Mater. Interfaces 6 (2014) 450–458.
[31] S. Joseph, B. Mathew, Mater. Sci. Eng. B 195 (2015) 90–97.
[32] M. Govindasamy, S.F. Wang, W.C. Pan, et al., Ultrason. Sonochem. 56 (2019) 193–199.
[33] M. Kaur, C. Sharma, N. Sharma, B. Jamwal, S. Paul, ACS Appl. Nano Mater. 3 (2020) 10310–10325.
[34] M. Chen, N. Wang, X. Wang, Y. Zhou, L. Zhu, Chem. Eng. J. 413 (2021) 127539.
[35] S. Zhang, J. Ye, Z. Liu, et al., Dalton Trans. 49 (2020) 13044–13051.
[36] Y. Zhang, X. Wang, Y. Wang, N. Xu, X.L. Wang, Polyoxometalates 1 (2022) 9140004.
[37] B. Das, M. Sharma, C. Kashyap, et al., Appl. Catal. A: Gen. 568 (2018) 191–201.
[38] F. Huang, E.V. Anslyn, Chem. Rev. 115 (2015) 6999–7000.
[39] J. Wang, S. Zhuang, Crit. Rev. Environ. Sci. Technol. 47 (2017) 2331–2386.
[40] M. Zeng, K. Chen, J. Tan, J. Zhang, Y. Wei, et al., Front. Chem. 6 (2018) 457.
[41] A.N. Chishti, F. Guo, A. Aftab, et al., Appl. Surf. Sci. 546 (2021) 149070.
[42] K.H. Choi, J. Min, S.Y. Park, B.J. Park, J.S. Jung, Ceram. Int. 45 (2019) 9477–9482.
[43] X. Deng, W. Li, G. Ding, X. Chen, Analyst 143 (2018) 2665–2673.
[44] P. Smaragdis, C. Fevotte, G.J. Mysore, N. Mohammadiha, M. Hoffman, IEEE Signal Process. Mag. 31 (2014) 66–75.
[45] A.L. Bugaev, V.A. Polyakov, A.A. Tereshchenko, et al., Metals 8 (2018) 135.
[46] S. Sharma, C. Sharma, M. Kaur, S. Paul, New J. Chem. 45 (2021) 20309–20322.
[47] S. Poulin, R. Franca, L. Moreau-Bélanger, E. Sacher, J. Phys. Chem. C 114 (2010) 10711–10718.
[48] M. Akia, N. Salinas, S. Luna, et al., J. Mater. Sci. 54 (2019) 13479–13490.
[49] D. Wilson, M. Langell, Appl. Surf. Sci. 303 (2014) 6–13.
[50] Y. Xu, K. Han, J. Xiang, X. Wang, IEEE Acc. 8 (2020) 159162–159171.
[51] D. Zhang, Z. Liu, S. Han, et al., Nano Lett. 4 (2004) 2151–2155.
[52] S. Liu, Y.T. Li, X.C. Zheng, et al., Int. J. Hydrog. Energy 45 (2020) 1671–1680.
[53] C. Du, P. Li, F. Yang, et al., ACS Appl. Mater. Interfaces 10 (2018) 753–761.
[54] F. Vitale, I. Fratoddi, C. Battocchio, et al., Nanoscale Res. Lett. 6 (2011) 1–9.
[55] M. Khoobi, T.M. Delshad, M. Vosooghi, et al., J. Magn. Magn. Mater. 375 (2015) 217–226.
[56] J. Xu, C. Ju, J. Sheng, et al., Bull Korean Chem. Soc. 34 (2013) 2408–2412.
[57] A.D. Aderibigbe, R.A. Crane, M.R. Lees, A.J. Clark, J. Nanoparticle Res. 22 (2020) 1–14.
[58] X. Zhang, X. Zhang, R.P. Feng, L.H. Liu, H. Meng, Mater. Chem. Phys. Mater. 136 (2012) 555–560.
[59] S.W. Chook, C.H. Chia, C.H. Chan, et al., RSC Adv. 5 (2015) 88915–88920.
[60] Z.J. Jiang, C.Y. Liu, L.W. Sun, J. Phys. Chem. 109 (2005) 1730–1735.
[61] V. Vidhu, D. Philip, Micron 56 (2014) 54–62.
[62] S.K. Ghosh, S. Kundu, M. Mandal, T. Pal, Langmuir 18 (2002) 8756–8760.
[63] S. Rajalakshmi, S. Pitchaimuthu, N. Kannan, P. Velusamy, J. Phys. Chem. Solids 165 (2022) 110691.
[64] H. Mittal, S.B. Mishra, Gum Ghatti, Carbohydr. Polym. 101 (2014) 1255–1264.
[65] X. Zhang, H. Zheng, S. Jin, et al., J. Solid State Chem. 293 (2021) 121802.
[66] P. Xu, C. Cen, M. Zheng, et al., Chem. Phys. Mater. 253 (2020) 123444.
[67] E. Murugan, J.N. Jebaranjitham, Chem. Eng. J. 259 (2015) 266–276.
[68] H. Veisi, S.B. Moradi, A. Saljooqi, P. Safarimehr, Mater. Sci. Eng. C 100 (2019) 445–452.
[69] X. Cui, Y. Zheng, M. Tian, Z. Dong, Appl. Surf. Sci. 416 (2017) 103–111.
[70] M. Nasrollahzadeh, S.M. Sajadi, A. Hatamifard, Appl. Catal. B 191 (2016) 209–227.
[71] Y. Ling, M. Zhang, J. Zheng, et al., Dalton Trans. 47 (2018) 7839–7847.
[72] A.N. Chishti, Z. Ma, Y. Liu, et al., Colloid Suf. A: Physicochem. Eng. Asp 631 (2021) 127694.